



Influence of the microstructure on the bulk and grain boundary conductivity in apatite-type electrolytes

D. Marrero-López^{a,*}, L. dos Santos-Gómez^b, L. León-Reina^c, J. Canales-Vázquez^d, E.R. Losilla^b

^aDepartment of Applied Physics I, University of Málaga, 29071 Málaga, Spain

^bDepartment of Inorganic Chemistry, University of Malaga, 29071 Malaga, Spain

^cServicios Centrales de Apoyo a la Investigación, University of Málaga, 29071 Malaga, Spain

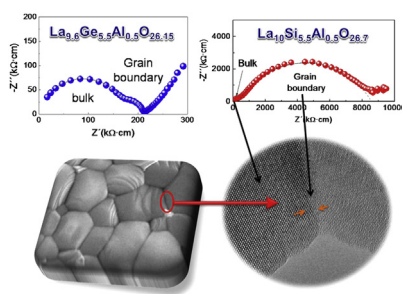
^dRenewable Energy Research Institute, University of Castilla-La Mancha, 02071 Albacete, Spain



HIGHLIGHTS

- The bulk conductivity of silicate apatites depends on both porosity and sintering temperature.
- The bulk conductivity of silicates is more affected by the porosity than the grain boundary one.
- The conductivity of germanate apatites is little affected by the ceramic microstructure.

GRAPHICAL ABSTRACT



ARTICLE INFO

Article history:

Received 12 April 2013

Received in revised form

14 June 2013

Accepted 18 June 2013

Available online 27 June 2013

Keywords:

Apatite-type electrolyte

SOFC

Microstructure

Porosity

Impedance spectroscopy

ABSTRACT

Silicate and germanate apatites have attracted great interest because of their high ionic conductivity for fuel cells and other electrochemical applications. The values of conductivity of these materials are comparable or even higher than those of $Zr_{0.84}Y_{0.16}O_{1.92}$ (YSZ), but vary depending on the synthetic method used and the level of densification. In order to evaluate the influence of the microstructure on the transport properties of apatite-type electrolytes, $La_{10}Si_{5.5}Al_{0.5}O_{26.75}$ (LSA) and $La_{9.6}Ge_{5.5}Al_{0.5}O_{26.15}$ (LGA) ceramics with different porosity and average grain size were prepared by varying the sintering temperature and time. Impedance spectroscopy was used to study separately both the bulk and grain boundary contributions from the overall conductivity. The bulk and grain boundary conductivities of silicates resulted highly dependent on both the porosity and the sintering temperature, on the contrary, the conductivity in germanates is barely affected by the microstructure.

© 2013 Elsevier B.V. All rights reserved.

1. Introduction

Ionic conductors based on silicates and germanates with apatite type structure are alternative electrolytes to the conventional yttria-stabilized zirconia to operate in Solid Oxide Fuel Cells (SOFCs) in the intermediate temperature range (600–800 °C) [1–4]. The oxide ion conductivity in these materials occurs mainly via oxygen interstitials with preferential *c*-axis conduction in comparison to

* Corresponding author. Present address: Dpto. de Física Aplicada I, Laboratorio de Materiales y Superficies (Unidad Asociada al C.S.I.C.), Facultad de Ciencias, Campus de Teatinos, Universidad de Málaga, 29071 Málaga, Spain. Tel.: +34 952137057; fax: +34 952132382.

E-mail addresses: damarre@uma.es, marrero@uma.es (D. Marrero-López).

oxygen vacancy migration in fluorite and perovskite-based electrolytes [5–13].

The conductivity of several Ge-based apatites has been reported to be higher compared to the analogous silicates [14–20]. Nevertheless, silicates have been studied more extensively due to several problems related to the high cost of germanium and volatilization losses at high sintering temperatures [21]. One of the major limitations for practical application of apatite silicates lies on the difficulty in preparing dense ceramics. For instance, the archetype compound $\text{La}_{9.33}(\text{SiO}_4)_6\text{O}_2$ synthesized by conventional solid-state reaction requires sintering temperatures of 1600–1700 °C. In order to overcome this drawback, alternative sintering processes have been proposed such as hot-pressing technique and spark-plasma [22–25]. Another approach is to use precursor routes, e.g. reactive sintering, sol–gel, freeze–drying, etc., however, the sintering temperature necessary to obtain dense ceramics is still high (~1500–1600 °C) [26–40].

It is well-known that the conductivity of apatite silicates is highly dependent on the synthesis method and porosity as occurs in other solid electrolytes, e.g. BaZrO_3 , but these effects appear somewhat mitigated in the analogous germanates [18]. Focussing on the simplest oxyapatite stoichiometry, $\text{La}_{9.33}(\text{SiO}_4)_6\text{O}_2$, the reported conductivities for dense ceramics (>90% of relative density) vary in a broad range from 3.2×10^{-5} to $7.3 \times 10^{-3} \text{ S cm}^{-1}$ at 700 °C, depending on the synthesis method, temperature and the resulting densification and grain size [28–30].

The influence of the porosity on the electrical properties of $\text{La}_{9.33}(\text{SiO}_4)_6\text{O}_2$ has been investigated by Panteix et al. and surprisingly the grain interior resistance was more affected by the porosity than that of the grain boundary [24]. Dense samples with the same composition were prepared by Porras-Vázquez et al. using different methods (conventional, spark-plasma and reactive sintering) and the conductivity resulted to be seriously dependent on the synthesis route used [41].

Due to the difficulty to obtain dense apatites, a detailed study of the effects produced by both the porosity and grain size on the grain interior and grain boundary contributions to the conductivity of these materials has not yet been fully studied and understood. This requires samples prepared via the same synthetic method with different degree of porosity and grain size. Therefore, the aim of this work is to prepare lanthanum germanate and silicate apatites with controlled porosity and grain size by varying both the temperature and sintering time to obtain new insights of the role of the microstructure on the grain interior and grain boundary contributions of the conductivity. Small amounts of transition metals (e.g. Co, Cu, Al and Zn) were also used as sintering aids to improve the densification at lower temperature.

The compositions $\text{La}_{10}\text{Si}_{5.5}\text{Al}_{0.5}\text{O}_{26.75}$ (LSA) and $\text{La}_{9.6}\text{Ge}_{5.5}\text{Al}_{0.5}\text{O}_{26.15}$ (LGA) were chosen for this study because they exhibit high ionic conductivity without any phase transition in the whole temperature range studied (150–800 °C) [18,42–44].

2. Experimental

2.1. Synthesis

Polycrystalline powders of $\text{La}_{10}\text{Si}_{5.5}\text{Al}_{0.5}\text{O}_{26.75}$ (LSA) and $\text{La}_{9.6}\text{Ge}_{5.5}\text{Al}_{0.5}\text{O}_{26.15}$ (LGA) electrolytes were synthesized by a freeze–drying precursor method of stoichiometric cation solutions with ethylenediaminetetraacetic acid (EDTA) as complexing agent. Starting materials used as reagents were as follows: La_2O_3 (99.99%), SiO_2 (99.99%), amorphous GeO_2 (99.99%), $\text{Al}(\text{NO}_3)_3 \cdot 9\text{H}_2\text{O}$ (>99%) and EDTA (99.5%), supplied from Sigma–Aldrich. Lanthanum oxide was precalcined at 1000 °C for 2 h to achieve dehydration and decarbonation. Aluminium nitrate and germanium oxide, which

are hygroscopic, were previously studied by thermogravimetric analysis to determine the correct cation composition of these reagents.

The cation solutions were obtained through different procedures as a function of the tetravalent cation:

- i) A precursor of $\text{La}_{10}\text{Si}_{5.5}\text{Al}_{0.5}\text{O}_{26.75}$ (LSA) was firstly prepared by reaction sintering. Reagents were mixed for 1 h in a Fritsch ball mill (model Pulverisette 7) at 100 rpm with ethanol. The powders were dried at 60 °C, pelletized and then heated at 1300 °C for 5 h at a heating/cooling rate of 5 °C min⁻¹. Under these conditions, only partial reaction of the starting materials occurs. The pellet was ground in an agate mortar and dissolved in diluted nitric acid using a hot-plate with continuous stirring. The mixture of reactants was firstly heated because silica is not soluble in nitric acid, whereas the intermediate compounds formed at high temperature are soluble in acid. After that, an aqueous stoichiometric cation solution was obtained adding EDTA in a ligand:metal molar ratio of 1:1. The solution pH was adjusted to 7 by adding ammonia. The volume and cation concentration of the resulting solution were about 200 ml and 0.12 M of La^{3+} respectively. This solution was dropped and frozen in liquid nitrogen and the resulting ice crystals were dehydrated by vacuum sublimation in a freeze–dryer for 2 days. The amorphous precursor powders were immediately calcined at 300 °C to prevent rehydration and to produce the combustion of the organic material. A second thermal treatment at 1100 °C was necessary in order to remove the residual organic species and to achieve crystallization of the compounds.
- ii) Precursor powders of $\text{La}_{9.6}\text{Ge}_{5.5}\text{Al}_{0.5}\text{O}_{26.15}$ (LGA) were prepared by dissolving the amorphous GeO_2 and $\text{Al}(\text{NO}_3)_3 \cdot 9\text{H}_2\text{O}$ in distilled water, whereas La_2O_3 was dissolved in diluted nitric acid. These solutions were mixed in stoichiometric amounts and EDTA was added in a 1.5:1 ligand:metal molar ratio. The dried precursor was obtained by freeze–drying as described previously. Further experimental details on the synthesis can be found elsewhere [45,46].

2.2. Powder diffraction

X-ray powder diffraction (XRD) patterns were collected with a X'Pert MDP PRO diffractometer (PANalytical) equipped with a Ge(111) primary monochromator and the X'Celerator detector, using $\text{CuK}\alpha_1$ radiation ($\lambda = 1.54059 \text{ \AA}$). The overall measurement time was approximately 4 h per pattern to have good statistics over the 10–100° (2θ) angular range, with 0.0167° step size. Rietveld refinements of the XRD patterns were performed using FULLPROF software [47]. The fits were performed using a pseudo-Voigt peak-shape function. In the final cycles, the usual profile parameters (scale factors, background coefficients, zero-points, half-width, pseudo-Voigt and asymmetry parameters for the peak-shape) were refined. The occupation numbers and isotropic temperature factors were refined separately due to their strong correlation.

2.3. Densification and microstructural characterization

Ceramic with different relative density and grain size were obtained by adjusting the sintering temperature and time. For this purpose, the polycrystalline powders of LGA and LSA calcined at 800 and 1100 °C respectively were uniaxially pressed at 125 MPa into disks of 10 mm of diameter and 1.5 mm of thickness and then sintered in the temperature range of 1400–1600 °C for LSA samples and 1000–1200 °C for LGA samples for times between 15 min and 5 h.

Different transition metals were used as sintering aids in order to decrease the densification temperature of the silicate. Consequently, the polycrystalline powders of LSA at 1100 °C were mixed with an ethanolic solution containing metal nitrates of Co, Cu, Al, Li and Zn in quantities between 5 and 20 mol%, dried in air and then calcined at 600 °C for 1 h to decompose the nitrates into oxides. After that, the powders were used to prepare ceramic pellets, which were sintered between 1100 and 1500 °C for 1 h.

The relative density of the pellets was calculated from the mass, volume of the sample and the crystallographic density obtained from the structural analysis by Rietveld refinement.

The microstructure of the sintered pellets was examined by using a JEOL SEM-6490LV scanning electron microscope. The samples were gold sputtered to prevent charging of the surface. Average grain size of sintered pellets was estimated from SEM micrographs using the linear intercept method from at least 50 random lines and three different micrographs with an image-analysis software [48].

Transmission Electron Microscopy (TEM) studies were performed on a Jeol JEM 2100 electron microscope operating at 200 kV and equipped with an EDS detector (Oxford Link). TEM specimens were prepared by dispersing the specimen powders in acetone and depositing few drops of the suspension on to a holey carbon-coated copper grid (EMS). TEM images were analysed using Digital Micrograph™ software from Gatan.

2.4. Electrical characterization

To carry out the electrical characterisation, Pt electrodes were formed on both surfaces of the sintered pellets at 800 °C for 1 h using Pt-ink. Impedance spectroscopy measurements were performed using a frequency response analyser (Solartron 1260) in static air in the 0.1 Hz–1 MHz frequency range with an ac signal of 100 mV. The spectra were acquired during the cooling process in air conditions between 800 and 150 °C with a dwell time of 30 min between consecutive measurements. Impedance spectra were fitted with equivalent circuits using the ZView program to study separately the grain interior and grain boundary components of the resistance [49].

3. Results

3.1. Phase formation and structure

Fig. 1 shows the evolution of the XRD patterns for LSA and LGA powders with the temperature. The LSA crystalline compound begins to form at 1000 °C with a significant fraction ~25 wt% of lanthanum oxide (**Fig. 1a**). After calcining at 1100 °C for 1 h the apatite type structure is the main crystalline phase with a minor fraction of ~2.5 wt.% of La₂O₃. A single apatite phase is obtained at 1200 °C and no appreciable differences are observed in the XRD patterns between 1200 and 1600 °C for sintering times ranging between 15 min and 5 h.

The germanate apatite (LGA) is a single phase after calcining the precursor powders at only 700 °C (**Fig. 1b**). Structural changes with the sintering temperature were not detected up to 1200 °C. However, prolonged annealing times above 1400 °C lead to the formation of the triclinic structure, which is attributed to Ge volatilisation [45].

The crystallite size, evaluated by the widths of the relevant diffraction peaks, takes a minimum value of 50 nm for LGA calcined at 700 °C and 75 nm for LSA calcined at 1100 °C.

The Rietveld refinements indicate that LSA and LGA materials crystallise in a hexagonal cell with space group *P*6₃/*m* (**Fig. 2**) in good agreement with previous reports [12,18], and without the presence of secondary phases.

The unit cells parameters obtained for samples sintered at different temperatures are given in **Table 1**. As can be observed the unit cell volume for LSA compounds are quite similar varying between 590.487 and 590.568 Å³. This suggests that structural and compositional differences between the samples are negligible in the temperature range studied. In the case of LGA specimens, the unit cell volume depends significantly on the sintering temperature. This anomalous behaviour could be ascribed to water uptake in germanates as demonstrated in previous works [45,50]. The data of **Table 1** clearly show that the unit cell volume decreases with the sintering temperature from 620.80 Å³ at 1000 °C to 618.04 Å³ at 1200 °C possibly due to ceramic grain growth and lower surface area for hydration. It should also be highlighted that La_{10-x}Ge_{5.5}Al_{0.5}O_{26.75-3x/2} compounds with *x* < 0.2 exhibit triclinic

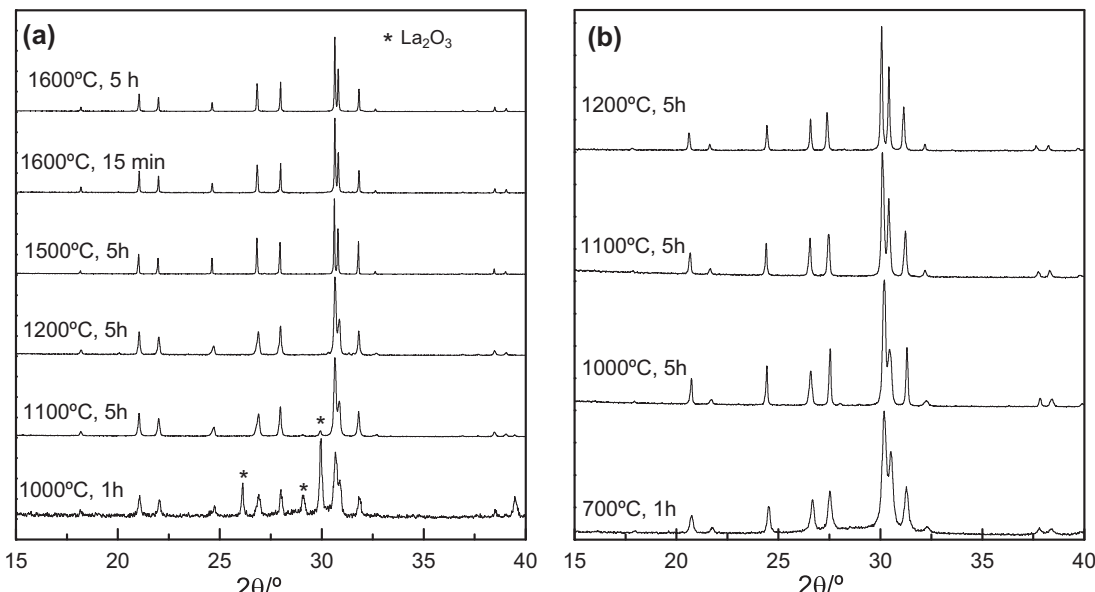


Fig. 1. XRD patterns as a function of the temperature for a) $\text{La}_{10}\text{Si}_{5.5}\text{Al}_{0.5}\text{O}_{26.75}$ and b) $\text{La}_{9.6}\text{Ge}_{5.5}\text{Al}_{0.5}\text{O}_{26.15}$.

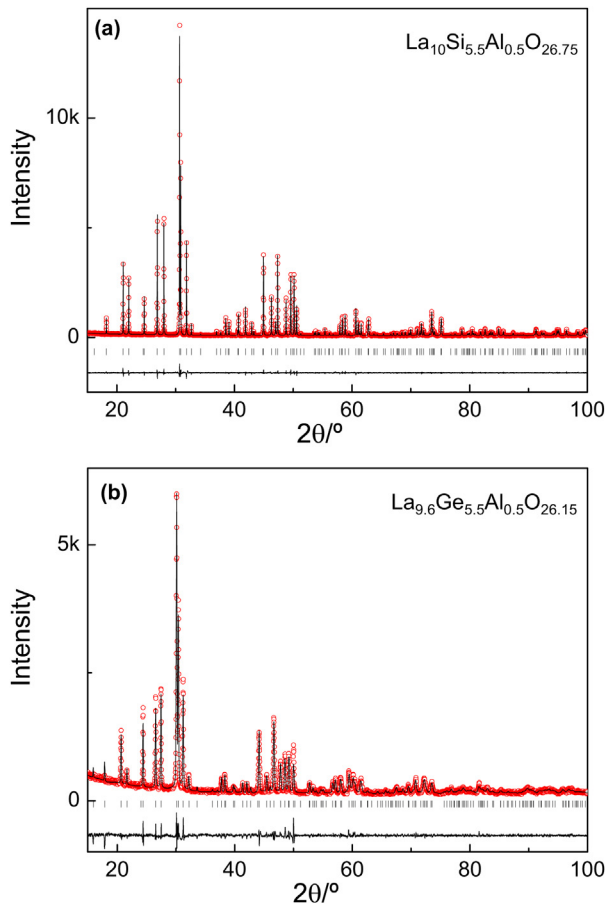


Fig. 2. Rietveld plots for a) $\text{La}_{10}\text{Si}_{5.5}\text{Al}_{0.5}\text{O}_{26.75}$ at 1400 °C and b) $\text{La}_{9.6}\text{Ge}_{5.5}\text{Al}_{0.5}\text{O}_{26.15}$ at 1100 °C.

structure (s.g. $P\bar{1}$) at room temperature with a phase transformation to hexagonal (s.g. $P6_3/m$) around 750 °C. The hydration of the triclinic phase results in the stabilization of the high temperature hexagonal polymorph [45,50].

3.2. HRTEM studies

The microstructure of the samples was investigated by electron diffraction and HRTEM image to obtain new insights on the bulk

Table 1

Sintering conditions, structural parameters, relative density ρ_r and average grain size D_g of $\text{La}_{10}\text{Si}_{5.5}\text{Al}_{0.5}\text{O}_{26.75}$ (LSA) and $\text{La}_{9.6}\text{Ge}_{5.5}\text{Al}_{0.5}\text{O}_{26.15}$ (LGA) ceramics.

Composition	Sintering temperature (°C)	a (Å)	c (Å)	V (Å 3)	ρ_r (%)	D_g (μm)
LGA	1000/5 h	9.9232 (1)	7.2797 (1)	620.80 (2)	75	0.5
	1050/5 h	9.9126 (2)	7.2838 (1)	619.82 (2)	82	0.6
	1100/5 h	9.9014 (2)	7.2852 (2)	618.54 (2)	90	0.7
	1150/5 h	9.8998 (3)	7.2867 (2)	618.47 (3)	95	0.95
	1200/5 h	9.8964 (3)	7.2867 (3)	618.04 (4)	98	1.1
LSA	1400/5 h	9.7258 (1)	7.2090 (1)	590.54 (6)	70	0.8
	1450/5 h	9.7261 (1)	7.2085 (1)	590.55 (3)	76	1.0
	1475/5 h	9.7248 (1)	7.2097 (1)	590.48 (2)	85	1.3
	1500/5 h	9.7245 (1)	7.2102 (1)	590.48 (1)	95	1.9
	1550/5 h	9.7236 (1)	7.2121 (1)	590.54 (2)	97	2.0
	1600/15 min	9.7216 (1)	7.2085 (1)	590.50 (1)	98	2.1
	1600/1 h	9.7244 (1)	7.2113 (1)	590.56 (2)	97	2.9
	1600/5 h	9.7298 (1)	7.2008 (1)	590.37 (1)	98	4.9

and grain boundary microstructure. No signs of phase segregation were observed in any of the samples in good agreement with the XRD results. In addition, no appreciable microstructural differences were found in the investigated samples. However, a very small fraction of silicate crystals exhibited the presence of nanodomains which may be responsible for variations in the bulk conductivity as discussed below (Fig. 3a).

Fig. 3b shows the SAED pattern and the corresponding HRTEM image recorded down the [001] direction for LGA sample. The reflections of the pattern can be indexed according to the hexagonal unit cell (s.g. $P6_3/m$) with $a = 9.7 \text{ \AA}$. The HRTEM image shows clearly the La/O channels in the c-axis where ion conduction dominates. The apatite structure along [001] direction is also displayed in the figure showing an excellent match with the real image.

HRTEM images also reveal clean and coherent grain boundaries and triple junctions without the presence of amorphous and/or phase segregations (Fig. 4). In addition, the grain boundary seems to have a thickness of only a few nanometres. These results seem to demonstrate that the high grain boundary resistance observed in apatite silicates can not be associated with a thick layer of amorphous silicon in the grain boundary region as previously suggested [41].

3.3. Ceramic microstructure

The microstructure evolution of LSA pellets with the temperature is shown in Fig. 5. Samples sintered below 1450 °C present a significant porosity, whereas those sintered at 1500 °C are nearly full dense. On the other hand, the time has little effects on the densification process as dense ceramics were obtained at 1600 °C for only 15 min and further grain growth is observed with the time (Fig. 5d–f).

The densification of LGA ceramics occurs at relatively low temperatures compared to silicates, i.e. ~90% at 1100 °C, and above this temperature only grain growth is observed (Fig. 6).

The cation stoichiometry of the pellets, determined using energy dispersive spectroscopy, confirmed essentially identical composition for the different samples in agreement with the XRD results.

Fig. 7 compares the evolution of the relative density and average grain size of LGA and LSA samples. It is observed that both relative density and average grain size increase with the temperature. LGA ceramics with relative density higher than 90% are obtained at 1100 °C, achieving complete densification around 1200 °C. LSA specimens require temperatures close to 1500 °C to achieve the same degree of densification. The high sintering temperatures required to obtain dense LSA ceramics leads to a significant grain growth compared to LGA. The average grain size in LGA ceramics

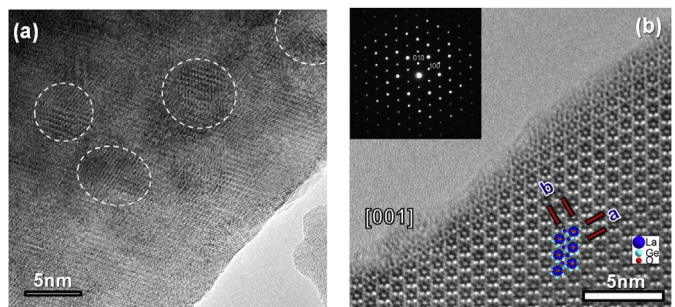


Fig. 3. a) HRTEM image for $\text{La}_{10}\text{Si}_{5.5}\text{Al}_{0.5}\text{O}_{26.75}$ sintered at 1500 °C showing the presence of nanodomains and b) SAED pattern and HRTEM image corresponding to the [001] zone-axes for the hexagonal $\text{La}_{9.6}\text{Ge}_{5.5}\text{Al}_{0.5}\text{O}_{26.15}$ compound. The inset shows the crystal structure views along the c-axis.

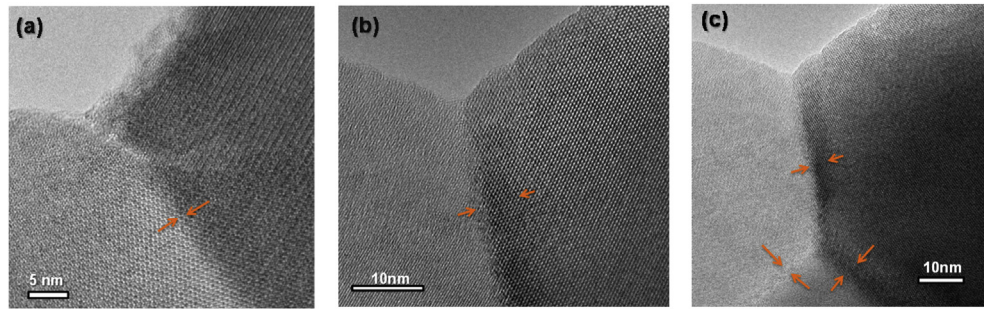


Fig. 4. HRTEM image in the grain boundary region of (a) $\text{La}_{9.6}\text{Ge}_{5.5}\text{Al}_{0.5}\text{O}_{26.15}$ and (b, c) $\text{La}_{10}\text{Si}_{5.5}\text{Al}_{0.5}\text{O}_{26.75}$ dense ceramics prepared at 1100 and 1500 °C respectively. Arrows indicate the grain boundary thickness.

increases with the temperature from 0.5 μm at 1000 °C to 1.1 μm at 1200 °C, whereas LSA ceramics show a larger variation between 0.8 μm at 1400 °C to 4.9 μm at 1600 °C (Table 1).

Metal transition cations, e.g. Co, Zn and Ni, are often used to improve the sintering of several materials, such as doped ZrO_2 , CeO_2 , BaZrO_3 and BaCeO_3 electrolytes [51–54]. The sintering enhancement in these ceramic materials is believed to take place as a result of enhanced diffusion through the grain boundary, possibly because of cation vacancy formation and/or liquid phases in the intergranular regions. An enhancement of the grain boundary conductivity has also been observed in these materials associated to lower segregation of the dopant at the grain boundary, lowering the corresponding space charge effects and the scavenging of insulating siliceous phases [55]. Following the same approach, LSA samples with different content (5–20 mol%) of sintering aids (Co, Cu, Al, Li and Zn) were sintered between 1200 and 1500 °C, however, dense ceramics with relative density higher than 90% were not obtained up to 1500 °C. Thus, these sintering aids do not improve the densification of silicate apatites and therefore these samples were not further characterized in this work. The exact role of these transition metals in the structure and the formation of secondary phases need to be further investigated to understand these results.

It should also be commented that the sinterability of $\text{La}_{10-x}\text{Si}_x\text{Al}_{0.5}\text{O}_{26.75}$ as well as the electrolyte conductivity could be improved by partial substitution of Ge by Si [32].

3.4. Electrical characterization

3.4.1. Bulk conductivity

The impedance spectra for LSA and LGA at different sintering temperatures indicate the presence of at least three different contributions (Fig. 8). The equivalent circuit used to fit the spectra consisted of two (RQ) elements and a pseudocapacitance in series. Hence, the equivalent circuit used to fit the data was: $(R_1Q_1)(R_2Q_2)(Q_3)$, which describes reasonably well the experimental data. The following parameters were obtained for each contribution: the resistance R_i , the pseudocapacitance Q_i and the exponential parameter n_i . The values of capacitance C_i were obtained from the following relation:

$$C_i = R_i^{(1/n_i-1)} \cdot Q_i^n \quad (1)$$

The high frequency contribution has capacitance values of 3 and 7 pF cm^{-1} for LGA and LSA samples respectively and can be assigned to the bulk, whereas the capacitance of the intermediate frequency contribution is around 1–4 nF cm^{-1} , which can be attributed to grain boundary component. Finally, the low frequency contribution is clearly related to the electrode processes.

The spectra of Fig. 8a for LGA show that the grain interior is the most important resistive contribution and the grain boundary is negligible for dense pellets prepared above 1150 °C. Furthermore, both bulk and grain boundary resistances change little with the

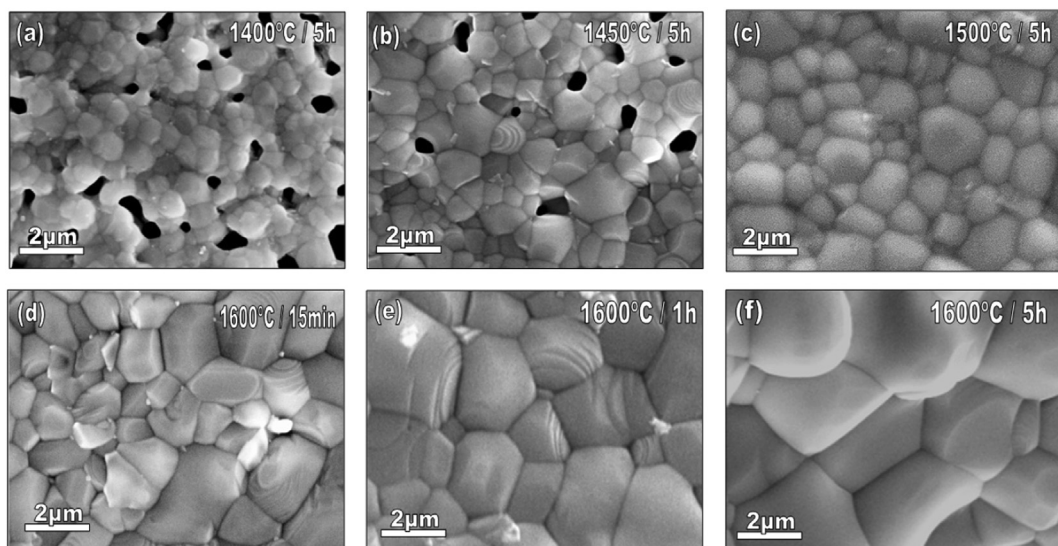


Fig. 5. SEM images of $\text{La}_{10}\text{Si}_{5.5}\text{Al}_{0.5}\text{O}_{26.75}$ ceramics sintered at different temperatures and times as detailed in each figure.

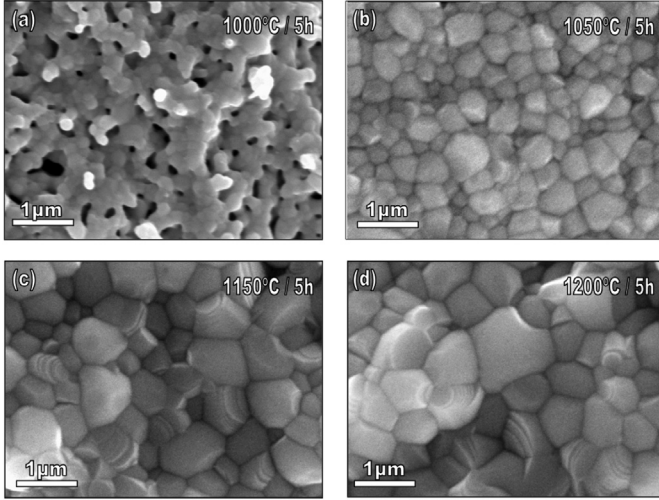


Fig. 6. SEM images of $\text{La}_{9.6}\text{Ge}_{5.5}\text{Al}_{0.5}\text{O}_{26.15}$ ceramics sintered at different temperatures and times as detailed in each figure.

degree of densification, even for samples with low relative density of 75%.

In LSA specimens, the grain boundary is the predominant contribution to the resistance. The bulk response is only visible at low temperatures ($T \leq 300$ °C) and very high frequencies (insets of Fig. 8b). Both bulk and grain boundary resistances decrease significantly with the temperature. This effect is more pronounced at sintering temperatures below 1475 °C due to the lower densification of the samples (<85%).

The grain interior R_b and grain boundary R_{gb} resistances were used to obtain the bulk and macroscopic grain boundary conductivities, taking into account the sample geometry:

$$\sigma_i = \frac{L}{R_i S} \quad (2)$$

where L and S are the thickness and electrode area of the pellets respectively.

The Arrhenius representation of the bulk conductivity is shown in Fig. 9a and b for LGA and LSA pellets respectively. It is observed that the bulk conductivity of LGA samples is nearly independent on

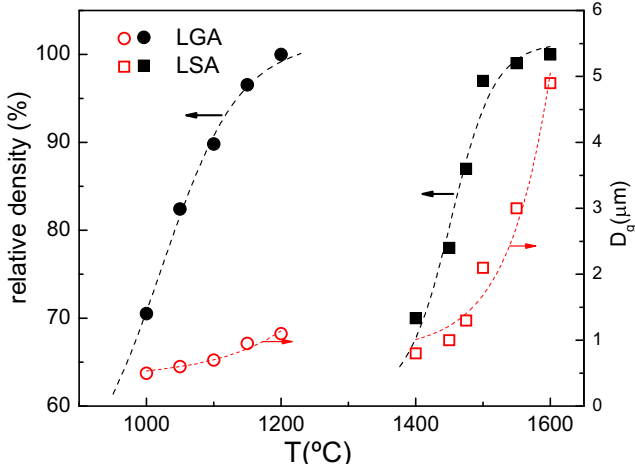


Fig. 7. Variation of relative density and average grain size with the sintering temperature for $\text{La}_{10}\text{Si}_{5.5}\text{Al}_{0.5}\text{O}_{26.75}$ (LSA) and $\text{La}_{9.6}\text{Ge}_{5.5}\text{Al}_{0.5}\text{O}_{26.15}$ (LGA) ceramics.

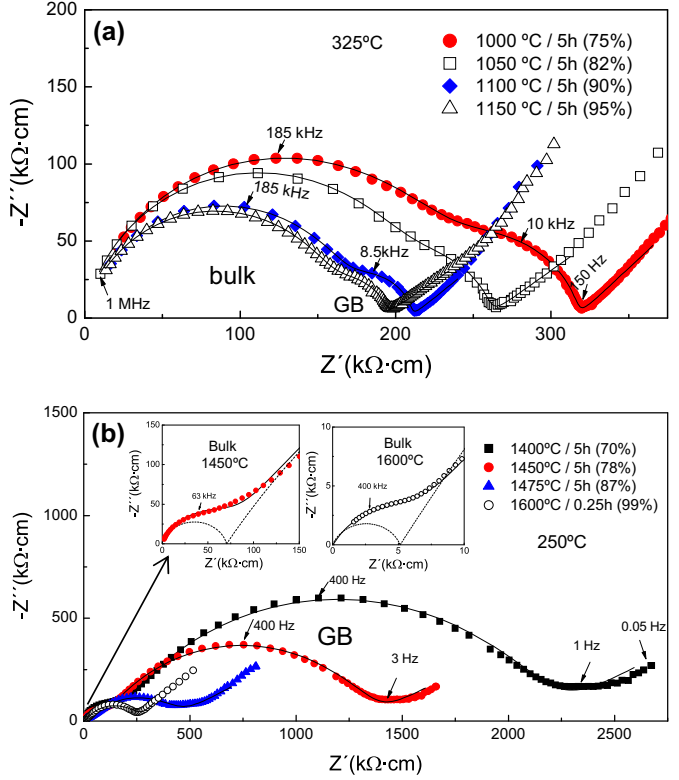


Fig. 8. Impedance spectra for (a) $\text{La}_{9.6}\text{Ge}_{5.5}\text{Al}_{0.5}\text{O}_{26.15}$ and (b) $\text{La}_{10}\text{Si}_{5.5}\text{Al}_{0.5}\text{O}_{26.75}$ pellets sintered at different temperatures and times as indicated in the figure and acquired at 325 and 250 °C respectively. The solid line is the fitting result with the equivalent circuit $(R_1Q_1)(R_2Q_2)(Q_3)$. The inset figures show a selected region of the impedance spectra at high frequency where the bulk contribution is visible.

the sintering temperature, despite the different relative densities (75–95%), varying between 8.2 and $13.6 \mu\text{S cm}^{-1}$ at 350 °C (Table 2). Note also that the porous materials seem to exhibit somewhat larger conductivity values in the low temperature region. The activation energies for bulk conduction are very similar for the different samples ~ 1.0 eV in the temperature range of 150–400 °C (Table 2).

LSA samples show a larger variation of the bulk conductivity, compared to germanates, increasing with the sintering temperature from 8.9 to $256 \mu\text{S cm}^{-1}$ at 250 °C for relative densities between 70 and 98% (Table 2). The difference is a factor of 30 and this could be mainly attributed to porosity because substantial compositional differences in the grain interior are ruled out by XRD analysis. However, the pellet prepared at 1500 °C with relative density of 95% exhibits lower bulk conductivity than those prepared at 1600 °C (Table 2), indicating that the bulk conductivity also depends on sintering temperature, in addition to the porosity. It should be noted that a similar behaviour was observed by Porras-Vázquez et al. in dense $\text{La}_{9.33}(\text{SiO}_4)_6\text{O}_2$ pellets sintered by spark-plasma at 1400 °C and reactive-sintering at 1650 °C with bulk conductivity values of 5.7 and $31 \mu\text{S cm}^{-1}$ respectively at 350 °C [41]. Furthermore, Li et al. also found a strong dependence of the bulk conductivity with the sintering temperature in $\text{La}_{10}\text{Si}_6\text{O}_{27}$, which was attributed to a better composition homogeneity as the temperature increases [56]. More recently, a variation of the conductivity was observed in $\text{Nd}_{(28+x)/3}\text{Al}_x\text{Si}_6-x\text{O}_{26}$ single crystals after long term annealing at 950 °C ascribed with the formation of domains with different Nd composition, and suggesting that the conductivity of apatite materials containing cation vacancies is affected by the thermal treatment [57]. It should be noted that

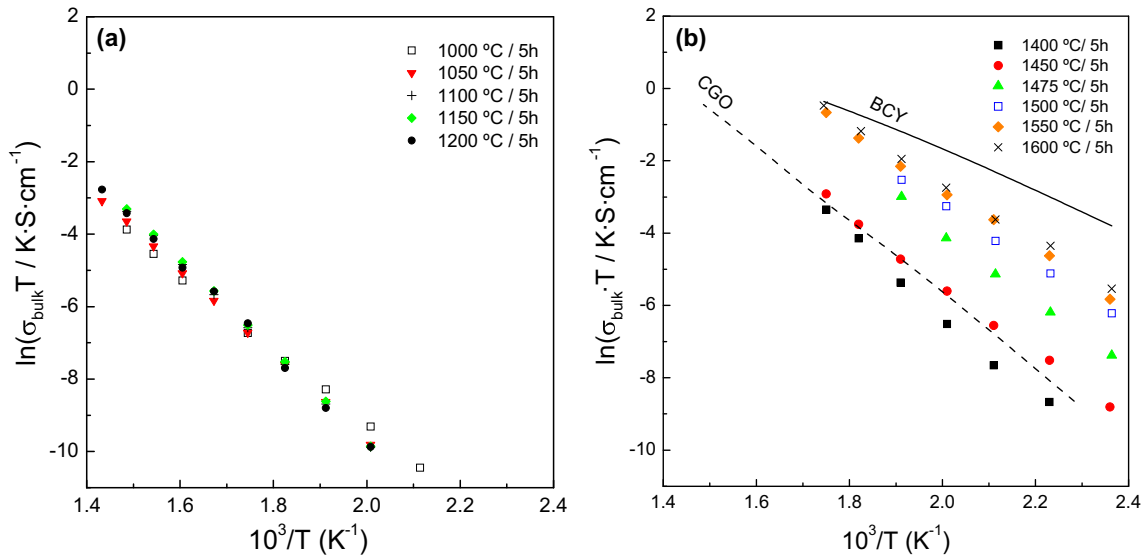


Fig. 9. Temperature dependence of the bulk conductivity for a) $\text{La}_{9.6}\text{Ge}_{5.5}\text{Al}_{0.5}\text{O}_{26.15}$ (LGA) and b) $\text{La}_{10}\text{Si}_{5.5}\text{Al}_{0.5}\text{O}_{26.75}$ (LSA) samples sintered at different temperatures. For comparison purpose the bulk conductivity of $\text{Ce}_{0.9}\text{Gd}_{0.1}\text{O}_{1.95}$ (CGO) and $\text{BaCe}_{0.9}\text{Y}_{0.1}\text{O}_{2.95}$ (BCY) electrolytes are included.

nanodomains were found in some crystals of the silicate apatite that could explain the different bulk conductivity with the sintering temperature. The presence of nanodomains in solid electrolytes, such as doped ceria, have been reported to be detrimental for the bulk conductivity [58,59]. Further microstructural studies by HRTEM are in progress to better understand the transport properties in the grain interior region of apatite silicates.

The activation energies for bulk conduction decrease with the sintering temperature from 0.85 eV at 1400 °C to 0.69 eV at 1600 °C (Table 2), following a linear relation with the porosity as previously observed for $\text{La}_{9.33}(\text{SiO}_4)_6\text{O}_2$ [24]. It is also remarkable to mention that the values of bulk conductivity for dense LSA samples are higher than those of $\text{Ce}_{0.9}\text{Gd}_{0.1}\text{O}_{1.95}$ (CGO) and comparable to those of proton conductors with perovskite structure such as $\text{BaCe}_{0.9}\text{Y}_{0.1}\text{O}_{2.95}$ (BCY). Taking into account that the grain-boundary is the predominant contribution to the resistance at low temperature in LSA samples, the reduction of this contribution would result in overall conductivity values substantially larger than CGO. This was the main reason to attempt to reduce the grain boundary resistance in LSA by the addition of transition metals.

3.4.2. Macroscopic grain boundary conductivity

The grain boundary resistances have been normalized by the grain size to take into account differences in the number of grain boundaries across the sample. This representation is proposed for cases when the brick-layer model provides quite satisfactory description for the dependence of grain boundary resistance on the grain size. The Arrhenius plots of the macroscopic grain-boundary resistance $L/(S \cdot R_{gb} \cdot D_g)$ for LGA and LSA samples are presented in Fig. 10a and b respectively. The grain boundary resistance for dense LGA samples is reasonably well described by the brick-layer model even for porous samples, although the activation energy increases with the sintering temperature from 1.15 eV at 1000 °C to 1.40 eV at 1200 °C. Thus the grain boundary conduction seems to be favoured in porous samples. This anomalous behaviour could be attributed to a different conduction mechanism at the grain boundary region. It should be commented that a significant increase of the conductivity was previously observed in humidified atmospheres for lanthanum germanates with low relative density of 80% [60], however, in a later work, no conductivity enhancement was observed in dense ceramics [45]. To confirm this, porous LGA

Table 2

Values of conductivity and activation energies for the bulk σ_b and grain boundary σ_{gb} contributions, total conductivity σ_t at 800 °C and grain boundary widths δ_{gb} for $\text{La}_{10}\text{Si}_{5.5}\text{Al}_{0.5}\text{O}_{26.75}$ (LSA) and $\text{La}_{9.6}\text{Ge}_{5.5}\text{Al}_{0.5}\text{O}_{26.15}$ (LGA) samples sintered at different temperatures.

Composition	Sintering temperature (°C)	E_{bulk} (eV)	E_{gb} (eV)	σ_b ($\mu\text{S cm}^{-1}$)	σ_{gb} ($\mu\text{S cm}^{-1}$)	$\sigma_t^{800^\circ\text{C}}$ (mS cm^{-1})	δ_{gb} (nm)
LGA	1000/5 h	0.89	1.15	8.2	0.35	9.65	5.2
	1050/5 h	1.00	1.28	10.0	0.32	12.1	6.3
	1100/5 h	1.08	1.26	12.7	0.30	15.3	3.5
	1150/5 h	1.08	1.30	13.6	0.31	16.4	3.2
	1200/5 h	1.07	1.40	11.6	—	16.8	—
LSA	1400/5 h	0.85	1.05	8.9	0.013	4.6	9.9
	1450/5 h	0.82	1.00	17.4	0.017	7.3	10.2
	1475/5 h	0.82	0.96	35.1	0.019	11.2	10.5
	1500/5 h	0.76	0.90	139	0.029	20.0	7.8
	1550/5 h	0.73	0.90	218	0.025	25.8	7.0
	1600/15 min	0.60	0.88	209	0.018	29.3	6.7
	1600/1 h	0.65	0.89	256	0.021	39.4	6.5
	1600/5 h	0.69	0.87	236	0.020	46.4	6.8

Bulk and grain boundary conductivity values for LGA at 350 °C and LSA at 250 °C.

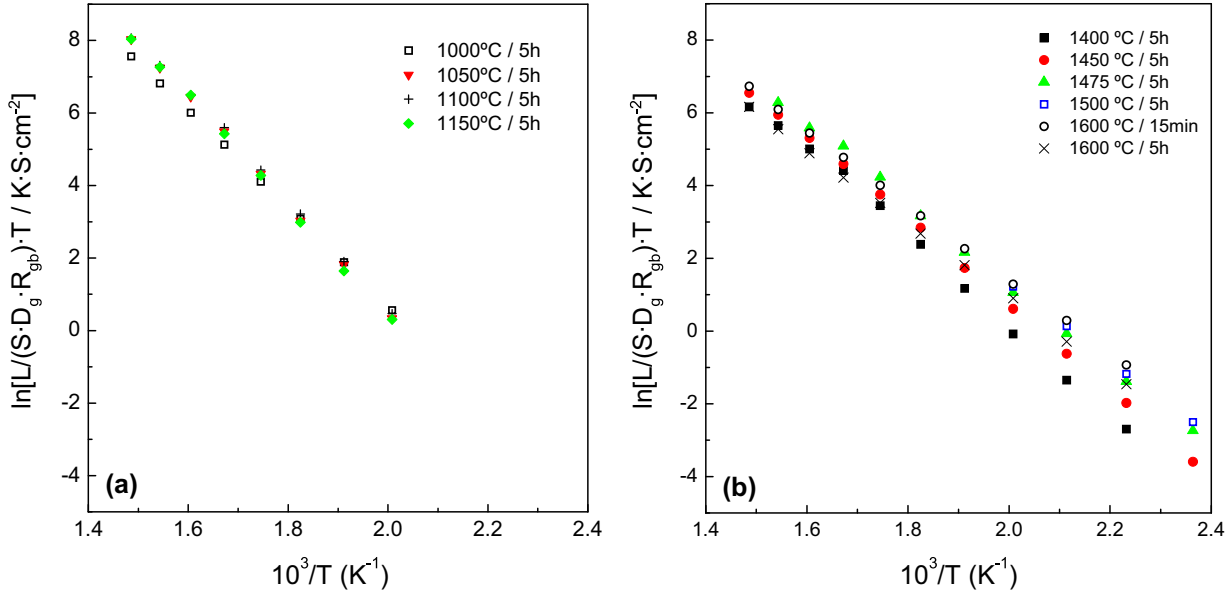


Fig. 10. Temperature dependence of the macroscopic grain boundary conductivity for a) $La_{9.6}Ge_{5.5}Al_{0.5}O_{26.15}$ (LGA) and b) $La_{10}Si_{5.5}Al_{0.5}O_{26.75}$ (LSA) samples sintered at different temperatures.

samples were measured by impedance spectroscopy under dry and wet N_2 ; and a decrease of the grain boundary resistance was observed in humidified atmosphere, indicating a possible proton conduction mechanism in this region. This might also explain the lower activation energy for the grain boundary conduction in porous germanate ceramics.

In LSA the grain boundary resistance for dense samples prepared above 1475 °C is relatively well described by the brick-layer model, although it fails for porous samples. The activation energy for the grain boundary conduction decreases slightly with the sintering temperature from 1.0 eV at 1400 °C to 0.9 eV at 1600 °C. These values are substantially larger than those observed in the grain interior region (Table 2).

3.4.3. Influence of the porosity on the bulk and grain boundary conductivities

The porosity dependence of the conductivity of a ceramic material could be described with Archie's law [61]:

$$\sigma_i = \sigma_i^0 [\text{vol}]^m \quad (3)$$

where σ_i is the apparent conductivity of the porous material, σ_i^0 the intrinsic conductivity of the dense material, $[\text{vol}]$ the volume fraction of the porous matrix, which corresponds to the relative density ρ_r and m is an exponential factor.

The bulk conductivity for LGA and LSA pellets as a function of relative density is shown in Fig. 11. LGA samples exhibit a linear dependence with values of slope m varying between 1.42 and 2.0 (Fig. 11a). These values are similar to those reported previously for other solid electrolytes, such as porous YSZ and CGO with m in the range of 1.9–2.7 [62,63]. The same representation for LSA shows a linear relationship, except for those samples with high relative density $>95\%$ and sintered above 1500 °C, which exhibit an abrupt conductivity increase (Fig. 11b). The m values are significantly larger than those of germanates, decreasing with the sintering temperature from 11.2 at 175 °C to 9.0 at 250 °C. This means that the bulk conductivity in the silicates is more affected by the porosity than in

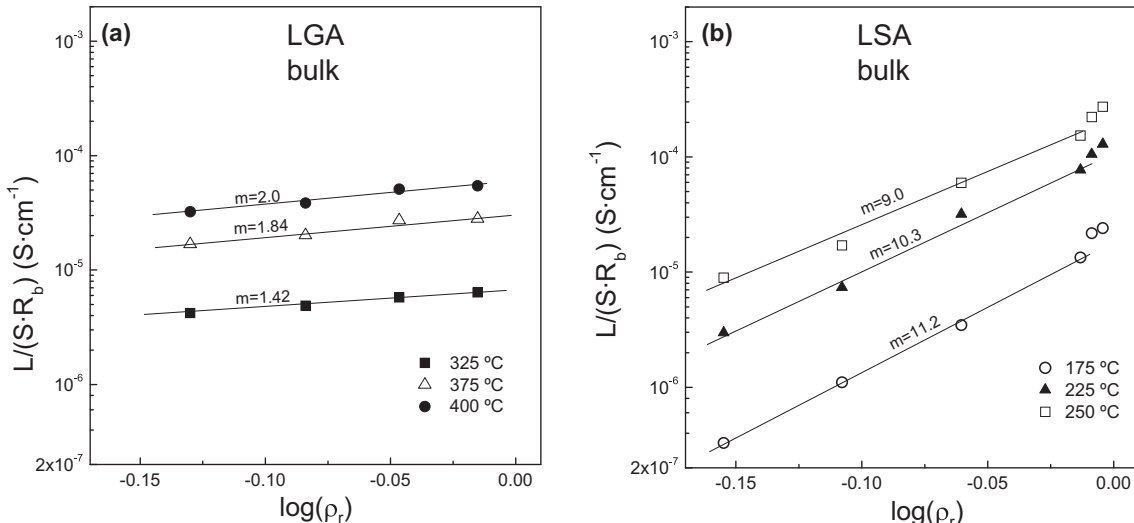


Fig. 11. Dependence of the bulk conductivity with the relative density ρ_r for a) $La_{9.6}Ge_{5.5}Al_{0.5}O_{26.15}$ (LGA) and b) $La_{10}Si_{5.5}Al_{0.5}O_{26.75}$ (LSA) samples at different temperatures.

the case of germanates. In addition, the decrease of m with the temperature indicates that the influence of porosity decreases when the temperature increases. It should be mentioned that high values of the exponential factor $m \sim 8.5$ at 400 °C were found for the overall conductivity of $\text{La}_{9.33}(\text{SiO}_4)_6\text{O}_2$ [24]. An analogous analysis for the macroscopic grain boundary resistance reveals a similar linear dependence with m values of 3.3–3.6 for LGA and 6.1–7.6 for LSA samples (Fig. 12a and b). It should be noted that the m values for the bulk conductivity of LSA are larger than those of the grain boundary, indicating that the porosity has stronger influence on the grain interior contribution than in the grain boundary, whereas an opposite behaviour was observed for germanates.

It should be commented that the porosity in conventional solid electrolytes, e.g. YSZ and CGO, usually has stronger effects on the grain boundary conduction, but the bulk conductivity for dense samples is nearly independent on the preparation method and temperature. In contrast, the bulk conductivity of silicate apatites depends on the preparation method, temperature as well as the porosity [24,41]. Thus the values of m are affected by all these factors. This anomalous behaviour could not be explained on the basis of significant structural differences as confirmed by XRD analysis. However, the presence of microstructural defects, such as nanodomains, composition inhomogeneities, which depend on the sintering temperature, may explain this behaviour but it needs to be confirmed by microstructural analysis.

3.4.4. Specific grain boundary conductivity

The macroscopic grain boundary conductivity calculated using Eq. (2) is not reliable because the thickness of the grain boundary parallel to the current flow is much smaller than that of the pellet (L/S). Thus, both the grain boundary layer thickness and grain size should be known to evaluate the specific grain boundary conductivity, defined as [64,65]:

$$\sigma_{gb} = \frac{\delta_{gb} \cdot N}{R_{gb} \cdot S} \approx \frac{L \cdot \delta_{gb}}{R_{gb} \cdot S \cdot D_g} \quad (4)$$

where N is the number of grain boundaries across the sample, δ_{gb} is the grain boundary layer width and D_g is the average grain size. The grain boundary layer thickness δ_{gb} must be known to obtain σ_{gb} and

can be obtained only by microscopy analysis. An alternative approach to estimate the grain boundary conductivity consists in the use of the bulk and grain boundary resistances and capacitances as follows [64,65]:

$$\sigma_{gb} = \frac{\epsilon_0 \epsilon_{gb}}{C_{gb} R_{gb}} \quad (5)$$

where ϵ_{gb} is the relative dielectric constant for the grain boundary and ϵ_0 is the vacuum dielectric constant. It is reasonable to take $\epsilon_{gb} \approx \epsilon_b$ under the assumption that the bulk and grain boundary regions are similar in both chemistry and atomic arrangement as confirmed by HRTEM measurements (Fig. 4), therefore assuming that grain boundary differences correspond mainly to changes in conductivity rather than differences in the dielectric constant as other authors have also assumed [65].

The relative dielectric constant was estimated by the bulk capacitances, which have been corrected by the stray capacitance, since the bulk capacitance with low S/L values are highly affected by the capacitance introduced by the experimental equipment with similar order of magnitude. The stray capacitance was obtained by determining the capacitance of a sample with known dielectric constant and different values of S/L .

The relative dielectric constants for dense pellets of LSA and LGA take values of 75 and 30 respectively. These values are somewhat larger than those reported previously $\epsilon_b \sim 15–25$ for polycrystalline pellets and single crystals of $\text{La}_{9.33}(\text{SiO}_4)_6\text{O}_2$ [24,66].

The temperature dependence of the specific grain boundary conductivity is plotted in Fig. 13a and b for LGA and LSA respectively. In LGA samples, the conductivity values are nearly independent on the sintering temperature (Fig. 13a). It is also remarkable to note that the grain boundary conductivity is slightly enhanced in the low temperature range for porous samples. This anomalous behaviour needs to be further investigated to clarify the dominant transport species (ion oxide and/or protons) at the grain boundary.

The specific grain boundary conductivity of dense LSA samples remains practically constant with the sintering temperature and is almost four orders of magnitude lower than that of the bulk (Table 2).

The grain boundary width δ_{gb} was estimated using the Eq. (6), which has been obtained by combining Eqs. (4) and (5):

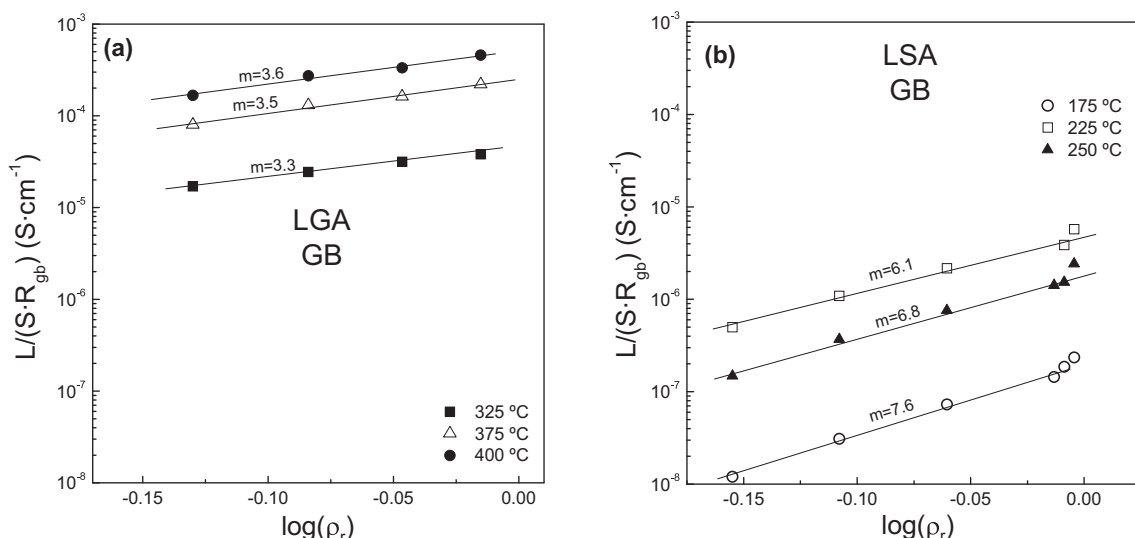


Fig. 12. Dependence of the grain boundary resistance with the relative density ρ_r for a) $\text{La}_{9.6}\text{Ge}_{5.5}\text{Al}_{0.5}\text{O}_{26.15}$ (LGA) and b) $\text{La}_{10}\text{Si}_{5.5}\text{Al}_{0.5}\text{O}_{26.75}$ (LSA) samples at different temperatures.

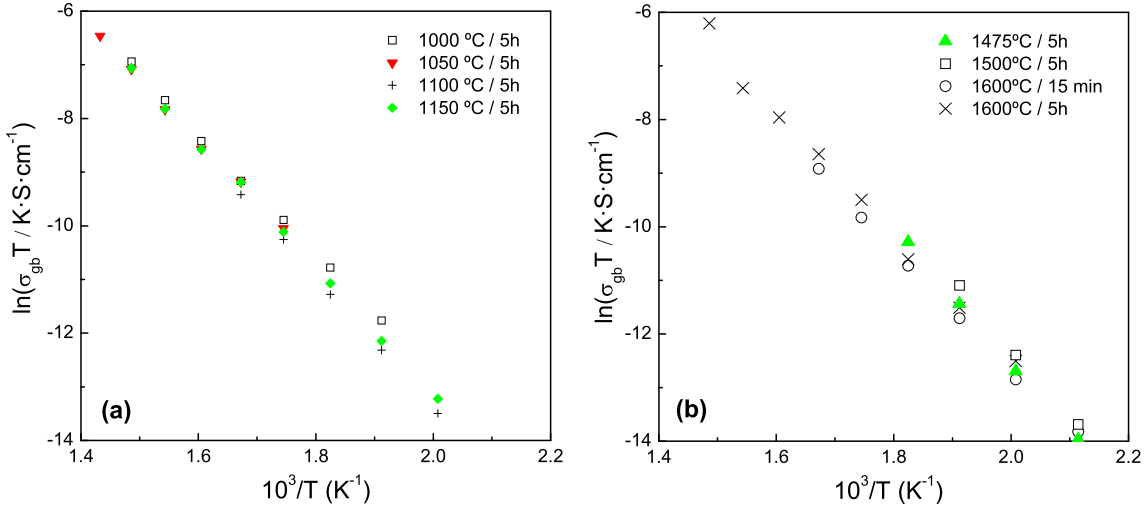


Fig. 13. Temperature dependence of the specific grain boundary conductivity of a) $\text{La}_{9.6}\text{Ge}_{5.5}\text{Al}_{0.5}\text{O}_{26.15}$ (LGA) and b) $\text{La}_{10}\text{Si}_{5.5}\text{Al}_{0.5}\text{O}_{26.75}$ (LSA) pellets sintered at different temperatures.

$$\delta_{gb} = \frac{\varepsilon_0 \varepsilon_b D S}{C_{gb} L} \quad (6)$$

The estimated grain boundary width for LGA samples ranged between 3 and 5 nm (Table 2). These values are similar to those found for other solid electrolytes (e.g. 1–2 nm for $\text{Ce}_{0.8}\text{Gd}_{0.2}\text{O}_{1.9}$ [55] and 3–4 nm for $\text{Zr}_{0.84}\text{Y}_{0.16}\text{O}_{1.92}$ [67]) and are in good agreement with HRTEM results (Fig. 4). The same estimation for LSA leads to somewhat larger grain boundary widths between 6.5 and 10.5 nm. This is possibly due to an overestimation of the dielectric constant in LSA samples with predominant grain boundary contribution in the impedance spectra.

3.4.5. Overall conductivity

The Arrhenius plots of the overall conductivity for LGA and LSA samples as a function of the sintering temperature are shown in

Fig. 14a and b respectively. The conductivity of LGA samples is not seriously affected by the sintering temperature and porosity with values varying between 9.7 and 16.8 mS cm⁻¹ at 800 °C and relative density of 75–95%.

On the contrary, LSA samples exhibit a larger variation in the overall conductivity increasing with the relative density in one order of magnitude from 4.6 to 46.5 mS cm⁻¹ at 800 °C for relative densities between 70 and 98% (Table 2). These differences in conductivity values are not only ascribed to porosity, as previously commented, because dense pellets of LSA prepared at 1600 °C for periods of time ranging between 15 min and 5 h also exhibit a significant variation in the conductivity, 29.3 and 46.5 mS cm⁻¹ respectively at 800 °C (Table 2). Li et al. have also reported an enhancement of the conductivity in $\text{La}_{10}\text{Si}_6\text{O}_{27}$ with the sintering temperature, which was attributed to a better homogeneity of the samples [56].

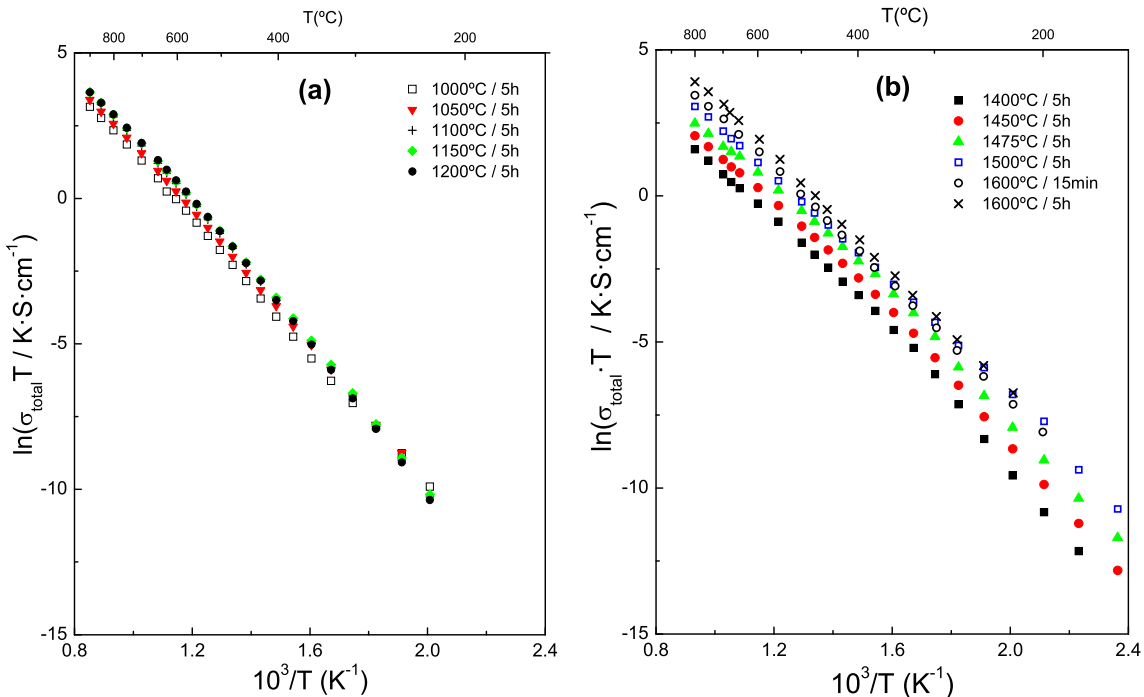


Fig. 14. Temperature dependence of the overall conductivity of a) $\text{La}_{9.6}\text{Ge}_{5.5}\text{Al}_{0.5}\text{O}_{26.15}$ (LGA) and b) $\text{La}_{10}\text{Si}_{5.5}\text{Al}_{0.5}\text{O}_{26.75}$ (LSA) pellets sintered at different temperatures.

Thus, the overall conductivity of silicate apatites depends on both the porosity and the sintering temperature, whereas germanates exhibit lower dependence of the conductivity on the microstructure. This explains the discrepancies reported in the literature regarding to the different conductivity values between germanate and silicate apatites.

4. Conclusions

Nanocrystalline powders of $\text{La}_{10}\text{Si}_{5.5}\text{Al}_{0.5}\text{O}_{26.75}$ (LSA) and $\text{La}_{9.6}\text{Ge}_{5.5}\text{Al}_{0.5}\text{O}_{26.15}$ (LGA) were prepared at low temperature by an alternative freeze-drying precursor route. These powders were used to obtain ceramic pellets with different degree of porosity and average grain size by varying the sintering temperature and time. The XRD and HRTEM studies confirmed that these samples present the same structure and composition independently on the sintering temperature, although occasionally nanodomain formation was observed in silicates that may have an impact in the bulk conductivity.

Small amounts of transition metals, i.e. Co, Cu, Al, Li and Zn used as sintering aids, do not improve the densification of silicate apatites at lower temperatures.

Impedance spectroscopy measurements were performed to evaluate the effects of the porosity and grain size on the bulk and grain boundary transport properties. For silicate apatites, the bulk conductivity depends on both the level of densification and sintering temperature. LSA samples with low level of densification show a linear relationship between the bulk conductivity and the relative density, following Archie's law, however, an abrupt increase in the bulk conductivity was observed after densification reached completion above 1500 °C. This indicates that the bulk conductivity of silicates depends on both porosity and sintering temperature. In addition, the bulk conductivity of silicate apatite is more affected by the porosity than the grain boundary one. In contrast, the bulk conductivity of germanates is little affected by the porosity even for samples with low relative density of 75%.

The macroscopy grain boundary resistance for dense ceramics is relatively well described by the brick-layer model. The specific grain boundary conductivity of silicate apatites is practically independent on the sintering temperature and is almost four orders of magnitude lower than that of the bulk. On the contrary, the grain boundary conduction in germanates enhances in porous samples due to a possible proton conduction mechanism through this region.

The values of overall conductivity for silicates increase with the level of densification and sintering temperature between 4.6 and 46 mS cm⁻¹ at 800 °C for relative densities in the range of 70–98%, whereas the germanates display lower dependence of the overall conductivity on the relative density ranging between 9.7 and 16.8 mS cm⁻¹ at 800 °C.

Acknowledgements

This work was supported by the Junta de Andalucía (Spain) through the P10-FQM-6680 research and the Spanish MINECO MAT2010-19837-C06-04.

References

- [1] A.J. Jacobson, Chem. Mater. 22 (2010) 660–674.
- [2] A. Orera, P.R. Slater, Chem. Mater. 22 (2010) 675–690.
- [3] L. Malavasi, C.A.J. Fisher, M.S. Islam, Chem. Soc. Rev. 39 (2010) 4370–4387.
- [4] D. Marrero-López, M.C. Martín-Sedeño, J. Peña-Martínez, J.C. Ruiz-Morales, P. Núñez, M.A.G. Aranda, J.R. Ramos-Barrado, J. Power Sources 195 (2010) 2496–2506.
- [5] J.R. Tolchard, M.S. Islam, P.R. Slater, J. Mater. Chem. 13 (2003) 1956–1961.
- [6] M.S. Islam, J.R. Tolchard, P.R. Slater, Chem. Commun. (2003) 1486–1487.
- [7] E. Kendrick, M.S. Islam, P.R. Slater, Chem. Commun. (2008) 715–717.
- [8] E. Kendrick, M.S. Islam, P.R. Slater, J. Mater. Chem. 17 (2007) 3104–3111.
- [9] K. Fukuda, T. Asaka, R. Hamaguchi, T. Suzuki, H. Oka, A. Berghout, O. Masson, I. Julien, E. Champion, P. Thomas, Chem. Mater. 23 (2011) 5474–5483.
- [10] E.J. Abram, D.C. Sinclair, A.R. West, J. Mater. Chem. 11 (2001) 1978–1979.
- [11] E. Kendrick, M.S. Islam, P.R. Slater, Solid State Ionics 177 (2007) 3411–3416.
- [12] L. León-Reina, E.R. Losilla, M. Martínez-Lara, S. Bruque, M.A.G. Aranda, J. Mater. Chem. 14 (2004) 1142–1149.
- [13] S. Nakayama, M. Higuchi, J. Mater. Sci. Lett. 20 (2001) 913–915.
- [14] S. Nakayama, M. Sakamoto, J. Mater. Sci. Lett. 20 (2001) 1627–1629.
- [15] P. Berastegui, S. Hull, F.J.G. García, J. Grins, J. Solid State Chem. 168 (2002) 294–305.
- [16] H. Arikawa, H. Nishiguchi, T. Ishihara, Y. Takita, Solid State Ionics 136–137 (2000) 31–37.
- [17] J.R. Tolchard, J.E.H. Sansom, P.R. Slater, M.S. Islam, J. Solid State Electrochem. 8 (2004) 668–673.
- [18] L. León-Reina, E.R. Losilla, M. Martínez-Lara, M.C. Martín-Sedeño, S. Bruque, P. Núñez, D.V. Sheptyakov, M.A.G. Aranda, Chem. Mater. 17 (2005) 596–600.
- [19] P.R. Slater, J.E.H. Sansom, J.R. Tolchard, M.S. Islam, Solid State Phenom. 195 (2003) 90–91.
- [20] A. Orera, T. Baikie, P. Panchmatia, T.J. White, J. Hanna, M.E. Smith, M.S. Islam, E. Kendrick, P.R. Slater, Fuel Cells 11 (2011) 10–16.
- [21] J.E.H. Sansom, P.R. Slater, Solid State Ionics 167 (2004) 23–27.
- [22] H. Yoshioka, T. Mitsui, A. Mineshige, T. Yazawa, Solid State Ionics 181 (2010) 1707–1712.
- [23] W. Gao, H.-L. Liao, C. Coddet, J. Power Sources 179 (2008) 739–744.
- [24] P.J. Panteix, I. Julien, P. Abéard, D. Bernache-Assollant, Ceram. Int. 34 (2008) 1579–1586.
- [25] H.-C. Yao, J.-S. Wang, D.-G. Hu, J.-F. Li, X.-R. Lu, Z.-J. Li, Solid State Ionics 181 (2010) 41–47.
- [26] S. Tao, J.T.S. Irvine, Mater. Res. Bull. 36 (2001) 1245–1258.
- [27] Y. Masubuchi, M. Higuchi, T. Takeda, S. Kikkawa, J. Alloys Compd. 408–412 (2006) 641–644.
- [28] S. Célérier, C. Laberty, F. Ansart, P. Lenormand, P. Stevens, Ceram. Int. 32 (2006) 271–276.
- [29] A. Chesnaud, G. Dezanneau, C. Estournès, C. Bogicevic, F. Karolak, S. Geiger, G. Geneste, Solid State Ionics 179 (2008) 1929–1939.
- [30] A. Chesnaud, C. Bogicevic, F. Karolak, C. Estournès, G. Dezanneau, Chem. Commun. 15 (2007) 1550–1552.
- [31] A.V. Teterskii, S.Y. Stefanovich, N.Y. Turova, Inorg. Mater. 42 (2006) 294–302.
- [32] M. Santos, C. Alves, F.A.C. Oliveira, T. Marcelo, J. Mascarenhas, A. Cavaleiro, B. Trindade, J. Power Sources 231 (2013) 146–152.
- [33] J.M. Porras-Vázquez, E.R. Losilla, M.A.G. Aranda, I. Santacruz, Ceram. Int. 38 (2012) 1851–1858.
- [34] B. Li, J. Liu, Y. Hu, Z. Huang, J. Alloys Compd. 509 (2011) 3172–3176.
- [35] R. Serra, C. Alves, F.A.C. Oliveira, T. Marcelo, J. Mascarenhas, B. Trindade, Ceram. Int. 38 (2012) 5355–5361.
- [36] L. Zhang, H.Q. He, H. Wu, C.Z. Li, S.P. Jiang, Int. J. Hydrogen Energy 36 (2011) 6862–6874.
- [37] E. Jothinathan, K. Vanmeensel, J. Vleugels, O. Van der Biest, J. Eur. Ceram. Soc. 30 (2010) 1699–1706.
- [38] S.H. Jo, P. Muralidharan, D.K. Kim, J. Mater. Res. 24 (2009) 237–244.
- [39] E. Rodríguez-Reyna, A.F. Fuentes, M. Maczka, J. Hanuza, K. Boulahya, U. Amador, J. Solid State Chem. 179 (2006) 522–531.
- [40] S. Célérier, C. Laberty-Robert, F. Ansart, C. Calmet, P. Stevens, J. Eur. Ceram. Soc. 25 (2005) 2665–2668.
- [41] J.M. Porras-Vázquez, E.R. Losilla, L. León-Reina, D. Marrero-López, M.A.G. Aranda, J. Am. Ceram. Soc. 92 (2009) 1062–1068.
- [42] A.L. Shaula, V.V. Kharton, F.M.B. Marques, Solid State Ionics 177 (2006) 1725–1728.
- [43] V.V. Kharton, A.L. Shaula, M.V. Patrakeev, J.C. Waerenborgh, D.R. Rojas, N.P. Vyshatko, E.V. Tsipis, A.A. Yaremchenko, F.M.B. Marques, J. Electrochem. Soc. 151 (2004) A1236–A1246.
- [44] A.L. Shaula, V.V. Kharton, F.M.B. Marques, J. Solid State Chem. 178 (2005) 2050–2061.
- [45] D. Marrero-López, M.C. Martín-Sedeño, J.C. Ruiz-Morales, P. Núñez, J.R. Ramos-Barrado, Mater. Res. Bull. 45 (2010) 409–415.
- [46] D. Marrero-López, P. Díaz-Carrasco, J. Peña-Martínez, J.C. Ruiz-Morales, J.R. Ramos-Barrado, Fuel Cells 11 (2011) 65–74.
- [47] J. Rodríguez-Carvajal, Phys. B Condens. Matter 192 (1993) 55–69.
- [48] J.C.C. Abrantes, Estereología Software Package, ESTG/IPVC, Portugal, 2001.
- [49] D. Johnson, ZView Program, Versión 2.9b, Scribner Associates, Inc., Southern Pines, North Carolina, 1990–2005.
- [50] A. Orera, P.R. Slater, Solid State Ionics 181 (2010) 110–114.
- [51] C. Kleinlogel, L.J. Gauckler, Solid State Ionics 135 (2000) 567–573.
- [52] D.P. Fagg, J.C.C. Abrantes, D. Pérez-Coll, P. Núñez, V.V. Kharton, J.R. Frade, Electrochim. Acta 48 (2003) 1023–1029.
- [53] S. Tao, J.T.S. Irvine, Adv. Mater. 18 (2006) 1581–1584.
- [54] C. Peng, J. Melnik, J.-L. Luo, A.R. Sanger, K.T. Chuang, Solid State Ionics 181 (2010) 1372–1377.
- [55] D. Pérez-Coll, D. Marrero-López, P. Núñez, S. Piñol, J.R. Frade, Electrochim. Acta 51 (2006) 6463–6469.
- [56] B. Li, W. Liu, W. Pan, J. Power Sources 195 (2010) 2196–2201.

- [57] T. An, T. Baikie, F. Wei, S.S. Pramana, M.K. Schreyer, R.O. Piltz, J.F. Shin, J. Wei, P.R. Slater, T.J. White, *Chem. Mater.*, <http://dx.doi.org/10.1021/cm4000685>.
- [58] T. Mori, Y. Wang, J. Drennan, G. Auchterlonie, J.-G. Li, T. Ikegami, *Solid State Ionics* 175 (2004) 641–649.
- [59] F. Ye, T. Mori, D.-R. Ou, J. Zou, J. Drennan, *Solid State Ionics* 180 (2009) 1414–1420.
- [60] L. León-Reina, J.M. Porras-Vázquez, E.R. Losilla, M.A.G. Aranda, *J. Solid State Chem.* 180 (2007) 1250–1258.
- [61] G.E. Archie, *Trans. AIME* 146 (1942) 54.
- [62] D. Pérez-Coll, E. Sánchez-López, G.C. Mather, *Solid State Ionics* 181 (2010) 1033–1042.
- [63] M.C. Steil, F. Thevenot, M. Kleitz, *J. Electrochem. Soc.* 144 (1997) 390–398.
- [64] T. Van Dijk, A.J. Burggraaf, *Phys. Status Solidi A* 63 (1981) 229–240.
- [65] J.C.C. Abrantes, J.A. Labrincha, J.R. Fraile, *J. Eur. Ceram. Soc.* 20 (2000) 1603–1609.
- [66] Y. Kim, D.-K. Shin, E.-C. Shin, H.-H. Seo, J.-S. Lee, *J. Mater. Chem.* 21 (2011) 2940–2949.
- [67] S.P.S. Badwal, J. Drennan, *J. Mater. Sci.* 22 (1987) 3231–3239.